npj | computational materials

Article

Published in partnership with the Shanghai Institute of Ceramics of the Chinese Academy of Sciences

https://doi.org/10.1038/s41524-025-01737-9

Ferromagnetic semiconductor nanotubes with room Curie temperatures

Jia-Wen Li[1], Gang Su[1,2,3,4] ✉ & Bo Gu[1,2] ✉

Realizing ferromagnetic semiconductors with high Curie temperature T_C remains a challenge in spintronics. Recent experiments have obtained some two-dimensional (2D) room temperature ferromagnetic metals, such as monolayers CrS_2 and VSe_2. Inspired by the recent experimental progress on the nanotubes based on 2D van der Waals non-magnetic transition-metal dichalcogenides, magnetic nanotubes based on monolayer ferromagnetic materials are highly possible. Here, by the density functional theory calculations, we proposed a way to obtain a high T_C ferromagnetic semiconductor in magnetic nanotubes. Some high T_C ferromagnetic semiconductors are predicted in the MX_2 nanotubes (M = V, Cr, Mn, Fe, Co, Ni; X = S, Se, Te), including CrS_2 and $CrTe_2$ zigzag nanotubes with a diameter of 18 unit cells, showing T_C above 300 K. In addition, due to the strain gradient in the walls of nanotubes, an electrical polarization at the level of 0.1 eV/Å inward of the radial direction is obtained. Our results propose a way to obtain high-temperature ferromagnetic semiconducting nanotubes based on experimentally obtained 2D high T_C ferromagnetic metals.

Ferromagnetic semiconductors integrate magnetic functionality into conventional semiconductor platforms, enabling novel spintronic devices capable of simultaneous spin and charge manipulation[1–19]. Within standard semiconductor architectures, these materials uniquely generate, control, and detect spin-polarized currents through engineered spin-orbit coupling and magnetic anisotropy. This synergy unlocks transformative applications, including spin injection masers for coherent terahertz emission[18,19]; circularly polarized light-emitting diodes with chirality-tunable output[10]; magnetic diodes and p-n junctions exhibiting rectification tunable by external fields[11–14]; magnetic tunnel junctions with enhanced spin-dependent tunneling ratios[15,16]; and spin valve structures for nonvolatile memory integration[17]. For practical implementation, such devices require ferromagnetic semiconductors with Curie temperature T_C above 300 K to ensure room-temperature operation. However, most ferromagnetic semiconductors exhibit T_C values below 200 K due to magnetic dilution and weak exchange interactions. This critical limitation impedes their technological viability.

In 2017, the successful synthesis of two-dimensional (2D) van der Waals ferromagnetic semiconductors CrI_3[20] and $Cr_2Ge_2Te_6$[21] in experiments has attracted extensive attention to 2D ferromagnetic semiconductors. According to Mermin–Wagner theorem[22], the magnetic anisotropy is essential to produce long-range magnetic order in 2D systems. Recently, with great progress of 2D magnetic materials in experiments, more 2D ferromagnetic materials have been obtained, such as some ferromagnetic semiconductors with T_C far below room temperature[23–27], and some ferromagnetic metals with high T_C above room temperature[28–43]. In addition, some ferromagnetic semiconductors with T_C above room temperature have been predicted based on theoretical calculations[44–53], while their synthesis remains a challenge.

Since the first report of carbon nanotubes (CNTs)[54], one-dimensional materials based on 2D sheets have attracted attention because of their unique mechanical and electrical properties due to their low-dimensional structures. The structures of CNTs consist of nanodimensions made up of rolled sheets of 2D graphite. There are many ways a sheet of graphite is rolled up to form a tube, such as zigzag, chiral, and armchair; these are the names given to different types and could be controlled in experiments[55,56]. In addition, the diameters of nanotubes could be as small as sub-nm level[57–61]. There are some applications of CNT[55,62–73], such as chemical sensors[64], biomedical[65–67], biosensors[71,73] and digital electronics[68,72], etc.

There are some studies of magnetic nanotubes[74–86]. They were prepared by adding magnetic particles to non-magnetic nanotubes such as CNT doped with magnetic atoms, or ferromagnetic materials such as Fe, Co, and alloys, etc[74–80]. The nonreciprocal spin waves were observed in magnetic nanotubes under magnetic field[79]. Ni-doped silicon nanotubes were reported to be room temperature ferromagnetic semiconductors with tiny saturation magnetization[80]. It has some interesting applications, such as a platform for studying the magnetochiral effect, drug delivery, sorbent, catalysis, sensor, and basic building blocks for future memory elements[76–79,86].

[1]Kavli Institute for Theoretical Sciences, University of Chinese Academy of Sciences, Beijing, China. [2]Physical Science Laboratory, Huairou National Comprehensive Science Center, Beijing, China. [3]School of Physical Sciences, University of Chinese Academy of Sciences, Beijing, China. [4]Institute of Theoretical Physics, Chinese Academy of Sciences, Beijing, China. ✉e-mail: gsu@ucas.ac.cn; gubo@ucas.ac.cn

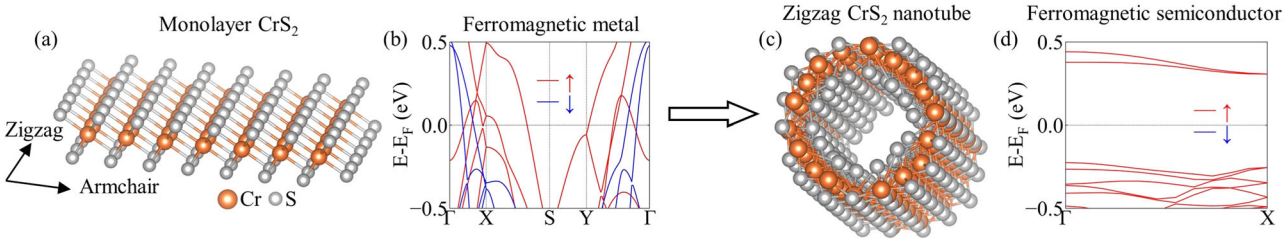

Fig. 1 | Metal-semiconductor transition in CrS_2 from monolayer to zigzag nanotube. a Crystal structure of monolayer CrS_2. **b** Spin-polarized band structure of monolayer CrS_2, demonstrating metallic behavior. **c** Crystal structure of zigzag CrS_2 nanotube. **d** Spin-polarized band structure of the zigzag CrS_2 nanotube, demonstrating semiconducting behavior.

Theoretical studies have demonstrated that magnetic nanotubes exhibit unique magnetic properties, including distinct spin-wave dynamics, domain wall propagation, unidirectional magnonic waveguiding, etc[81–85].

With the fast development of 2D van der Waals transition-metal dichalcogenides (TMD) materials, there are many experiments of TMD nanotubes[87–96], including WS_2[92–94,96], WSe_2[91], and MoS_2[89,97]. They show interesting properties, such as superconductivity[92,93] and photovoltaic effect[94,96]. In addition, some density functional theory (DFT) studies have investigated the properties of TMD nanotubes[98–107]. In this article, we theoretically predict high T_C ferromagnetic semiconducting nanotubes based on experimentally known 2D high T_C ferromagnetic metals. Considering the high T_C in experiments, ferromagnetic monolayers 1T-MX_2 (M = V, Cr, Mn, Fe, Co, Ni; X = S, Se, Te) were chosen as the initial 2D material to roll up. The DFT calculations were performed to investigate the properties of armchair and zigzag nanotubes with different diameters. We predicted some ferromagnetic semiconducting nanotubes with T_C above 200 K, including zigzag CrS_2 nanotube with 18 CrS_2 units (Z-18-CrS_2) showing T_C of 364 K and band gap of 0.53 eV, and Z-18-$CrTe_2$ showing T_C of 441 K and band gap of 0.16 eV. From monolayer cases to nanotube cases, they transition from high T_C ferromagnetic metals to high T_C ferromagnetic semiconductors. As shown in Fig. 1, monolayer CrS_2 is a ferromagnetic metal, whereas Z-18-CrS_2 is a ferromagnetic semiconductor. The stability of nanotubes is confirmed by the calculations of strain energy and molecular dynamics simulations. The strain energies of predicted nanotubes are lower than the experimentally prepared narrow MoS_2 nanotube, CNT, and BN nanotubes, suggesting the feasibility of preparation. Radial electric polarization at 0.1 eV/Å level is observed in nanotubes due to the strain gradient in the wall. As three representative results, the properties of CrS_2, $CrTe_2$, and VSe_2 nanotubes are discussed in detail in the paper. The properties of nanotubes are closely related to their diameter and structural configuration. Our theoretical results propose a way to obtain high T_C ferromagnetic semiconducting nanotubes derived from high T_C 2D ferromagnetic metals in experiments.

Results

Structures and stability of nanotubes

The crystal structure of monolayer CrS_2 is shown in Fig. 1a, with space group $P\bar{3}$ m1 (164). The calculated in-plane lattice constants are $a_0/\sqrt{3} = b_0 = 3.40$ Å, in agreement with previous calculation results of 3.28 Å[108]. The metallic band structure of monolayer CrS_2 is obtained by the DFT calculation, as shown in Fig. 1b. DFT calculation and Monte Carlo simulation results show that monolayer CrS_2 is a ferromagnetic metal with T_C of 295 K, close to the experimental results of T_C = 300 K[40]. Detailed calculation processes are given in Supplementary section 1 in Supplementary Material.

As shown in Fig. 1, zigzag and armchair nanotubes are obtained by rolling up monolayers along different directions[55]. The repeating MX_2 units in a unit cell of a nanotube are 12, 14, 16, 18, 20, 22, and 24, respectively. The diameter of nanotubes is defined according to the outer anions. Due to the different lattice constants of monolayer 1T-MX_2 along zigzag and armchair directions, armchair nanotubes exhibit larger diameters than their zigzag counterparts with the same number of atoms.

To analyze the stability of nanotubes, the strain energy E_{strain} is calculated by refs. 89,97,98,100,104,107

$$E_{strain} = \frac{E_{nanotube}}{N_{nanotube}} - \frac{E_{monolayer}}{N_{monolayer}}, \quad (1)$$

where $E_{nanotube}$, $E_{monolayer}$, $N_{nanotube}$, and $N_{monolayer}$ are the energies and total number of atoms in the nanotube and monolayer cases, respectively. Calculation results of E_{strain} of CrS_2, $CrTe_2$, and VSe_2 are shown in Fig. 2a. The positive E_{strain} indicates that the atoms in the nanotube possess higher energy than those in the monolayer, due to the strain induced by rolling up the monolayer. E_{strain} decreases with increasing diameter due to the decrease in strain. The detailed results of E_{strain} of zigzag and armchair nanotubes are listed in Table 1. The larger diameters of armchair nanotubes result in lower E_{strain} compared to zigzag nanotubes containing the same number of atoms. Armchair VSe_2 nanotubes with diameters exceeding 2.5 nm exhibit negative E_{strain}, suggesting the possibility of spontaneous curling. Similar positive results and behavior of E_{strain} are obtained in previous calculations[89,97,98,100,104,107]. CNTs with diameters <1 nm have been experimentally synthesized, exhibiting an E_{strain} exceeding 0.1 eV/atom[56–58]. Narrow h-BN nanotubes with a diameter of 0.45 nm were prepared and exhibited an E_{strain} of 0.25 eV/atom[61,109]. In addition, the single-walled MoS_2 nanotubes with a diameter of ~3.9 nm and E_{strain} of ~0.05 eV/atom were synthesized[97]. These experimental results support the stability of the nanotubes predicted in our calculations. It is worth noting that, even with different E_{strain}, the configuration and diameter of nanotubes can be controlled in experiments[55].

To further assess their stability, we performed molecular dynamics simulations on the Z-18-CrS_2 and Z-18-$CrTe_2$ nanotubes at 300 K using an NVT ensemble. Simulations were performed for 6 ps. The results presented in Fig. 3 provide key evidence for their dynamical stability. First, the total energy exhibits only minor oscillations around a stable baseline, indicating that the nanotubes are in thermal equilibrium. Moreover, the final atomic configurations, appearing distorted yet preserving the nanotube topology, confirm that the structures do not unravel, validating their room-temperature stability.

Band gap of nanotubes

The results of band gaps of zigzag CrS_2, $CrTe_2$, and VSe_2 nanotubes are shown in Fig. 2b. In monolayer cases, they are room temperature magnetic metals[40,42,43]. Non-zero band gaps were observed in zigzag nanotubes with some diameters. Zigzag CrS_2 nanotubes with diameters of 1.05 nm and 1.28 nm, zigzag VSe_2 nanotubes with diameters of 0.97 nm, 1.07 nm, 1.24 nm, and 1.69 nm, and zigzag $CrTe_2$ nanotubes with a diameter of 1.45 nm exhibited non-zero band gaps. The detailed results of band gaps of zigzag and armchair nanotubes are listed in Table 1. Nearly all armchair nanotubes display metallic behavior, except the armchair VSe_2 nanotube with a diameter of 1.46 nm, showing a band gap of 0.11 eV. Their band structure is given in Supplementary Figs. S3–S8 in the Supplementary Material. This configuration and perimeter-dependent electronic behavior

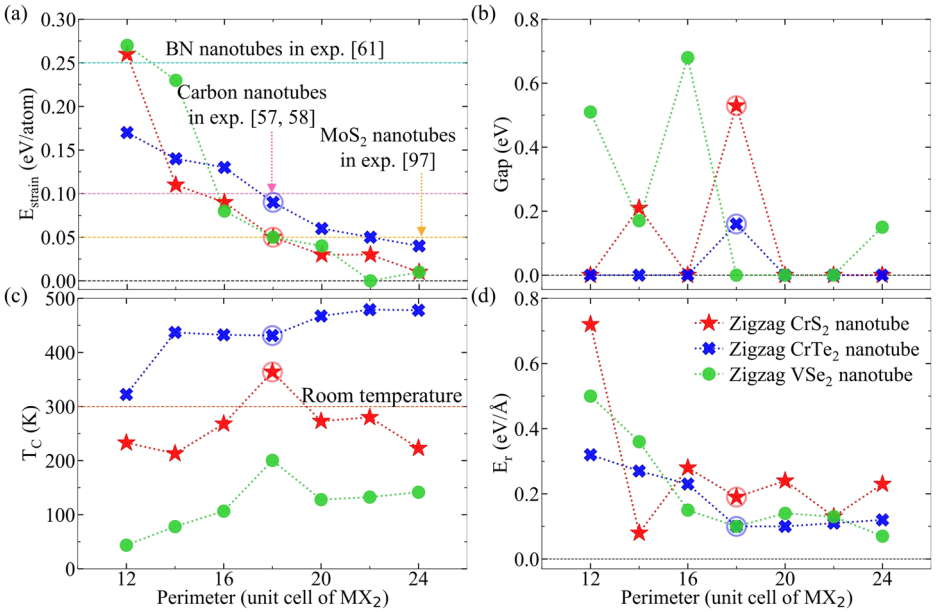

Fig. 2 | Calculated properties of zigzag CrS_2, $CrTe_2$ and VSe_2 nanotubes. a The results of strain energies E_{strain}. The E_{strain} of MoS_2 nanotubes with diameter of ~3.9 nm in experiment is ~0.05 eV/atom[97], of BN nanotubes with diameter of 0.45 nm is ~0.25 eV/atom[61], of CNT with diameter of 1 nm is ~0.10 eV/atom[57,58]. These values are shown for reference. **b** The results of band gaps. **c** Results of Curie temperatures T_C obtained by DFT calculation and Monte Carlo simulation. **d** The results of effective radial electrical field E_r inward along the radius. The results of room temperature ferromagnetic semiconductors of zigzag CrS_2 and $CrTe_2$ nanotubes are emphasized by circles.

Table 1 | The band gap, diameter, Curie temperature T_C, strain energy E_{strain} and radial electric field E_r inward along the radius for zigzag and armchair nanotubes

Structure		Zigzag					Armchair				
Material	Perimeter (MX_2 units)	Diameter (nm)	Gap (eV)	T_C (K)	E_{strain} (eV/atom)	E_r (eV/Å)	Diameter (nm)	Gap (eV)	T_C (K)	E_{strain} (eV/atom)	E_r (eV/Å)
CrS_2	12	0.92	0	233	0.26	0.72	1.38	0	286	0.07	0.09
	14	1.05	0.21	213	0.11	0.08	1.58		299	0.05	0.13
	16	1.14	0	268	0.09	0.28	1.71		329	0.02	0.25
	18	1.28	0.53*	364	0.05	0.20	1.88		275	0.02	0.14
	20	1.34	0	273	0.03	0.24	2.13		232	0.02	0.01
	22	1.46		280	0.03	0.13	2.34		309	0.02	0.00
	24	1.51		223	0.01	0.23	2.52		247	0.01	0.00
$CrTe_2$	12	1.08	0	322	0.17	0.32	1.58	0	375	0.11	0.16
	14	1.20		437	0.14	0.27	1.78		441	0.07	0.16
	16	1.31		432	0.13	0.23	1.99		323	0.04	0.15
	18	1.45	0.16*	431	0.09	0.10	2.21		318	0.02	0.13
	20	1.56	0	467	0.06	0.10	2.40		310	0.02	0.11
	22	1.66		479	0.05	0.11	2.61		291	0.01	0.11
	24	1.77		478	0.04	0.12	2.80		255	0.01	0.11
VSe_2	12	1.07	0.51	44	0.27	0.50	1.46	0.11	196	0.05	0.22
	14	1.64	0.17	78	0.23	0.36	1.64	0	209	0.01	0.21
	16	1.24	0.68	107	0.08	0.15	1.92		21	0.03	0.01
	18	1.34	0	200	0.05	0.10	2.12		25	0.01	0.01
	20	1.46		128	0.04	0.14	2.32		18	0.00	0.02
	22	1.57		133	0.00	0.13	2.53		15	−0.01	0.00
	24	1.69	0.15	141	0.01	0.07	2.73		114 (T_N)	−0.01	0.00

The results are obtained by DFT calculations and Monte Carlo simulations. Most band gaps are obtained by the DFT calculation with PBE functional, except the room temperature ferromagnetic semiconductors Z-18-CrS_2 and Z-18-$CrTe_2$ marked by * obtained with HSE functional.

indicate a metal-to-semiconductor transition influenced by structural deformation.

Similar to CNTs, TMD nanotubes exhibit a configuration and diameter-dependent metal-to-semiconductor transition[56,110]. For CNTs, some zigzag CNTs show a band gap while all armchair CNTs remain metallic; this behavior is attributed to the folding of the Brillouin zone, which depends on both configuration and diameter[56,110]. The configuration and perimeter-dependent metal-to-semiconductor transition in TMD nanotubes arises from two key effects: Brillouin zone folding and uniaxial strain. The top view and band structure of monolayer CrS_2 are

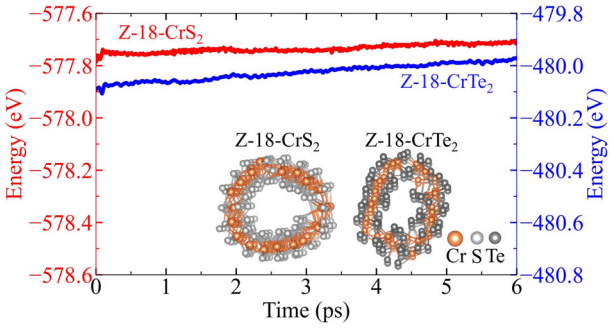

Fig. 3 | Molecular dynamics simulation results for Z-18-CrS_2 and Z-18-$CrTe_2$. The simulation was run at 300 K for 6 ps of molecular dynamics simulation results, energy and structure. Inside are the side views of crystal structures after 6 ps.

shown in Fig. 4a, b, respectively. Its Brillouin zone is shown in Fig. 4e. Figure 4f depicts the Fermi contour of monolayer CrS_2, defined as the locus of K points satisfying $E(k) = E_F$. The features of the Fermi contour agree with the band structure in Fig. 4b. The existence of a band gap along a specific K-path can be determined by examining whether there exist intersections of the Fermi contour with the corresponding path. Intersections are observed with the Γ-X, Γ-Y, and S-X paths, indicating no band gap along these directions. Conversely, the absence of intersections with the S-Y path indicates the presence of a band gap along this path.

The electronic properties of the monolayer are significantly affected by applied strain. To quantify strain, we define the strain ratio by $\epsilon = (a - a_0)/a_0 \times 100\%$, where a and a_0 are the lattice constants with and without strain, respectively. The band structure and Fermi contour of monolayer CrS_2 under 34% tensile strain along x direction are shown in Fig. 4b, g, respectively. Under this strain, no intersections are observed between the Fermi contour and the Γ-Y or S-X paths, implying the presence of energy gaps

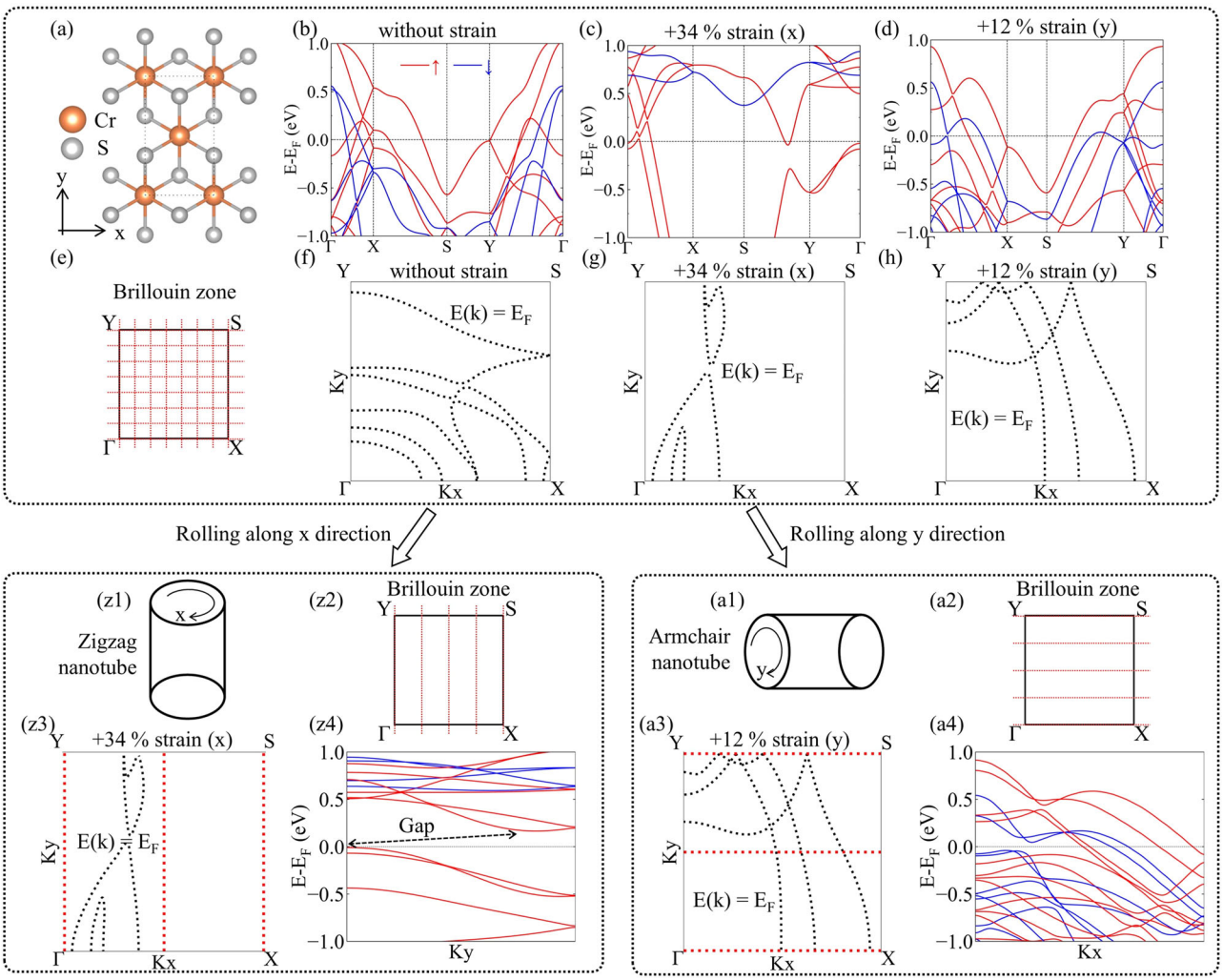

Fig. 4 | Analysis of band structure evolution in CrS_2 from monolayer to nanotubes. a Orthorhombic unit cell of monolayer CrS_2. **b–d** Band structures without strain (**b**), under 34% tensile strain along x direction (**c**), and under 12% tensile strain along y direction (**d**). **e** The 2D Brillouin zone of monolayer CrS_2. **f–h** Fermi contours at $E(k) = E_F$ without strain (**f**), under 34% tensile strain along x direction (**g**), and under 12% tensile strain along y direction (**h**). Schematic diagram of a zigzag nanotube (z1) and the corresponding 1D Brillouin zone (z2). (z3) The Fermi contour of monolayer CrS_2 under 34% tensile strain along x direction, lines parallel to Γ-Y represent the 1D Brillouin zone of zigzag nanotubes. (z4) The band structure corresponds to (z3). Schematic diagram of an armchair nanotube (a1) and the corresponding 1D Brillouin zone (a2). (a3) The Fermi contour of monolayer CrS_2 under 12% tensile strain along y direction, lines parallel to Γ-X represent the 1D Brillouin zone of armchair nanotubes. (a4) The band structure corresponds to (a3).

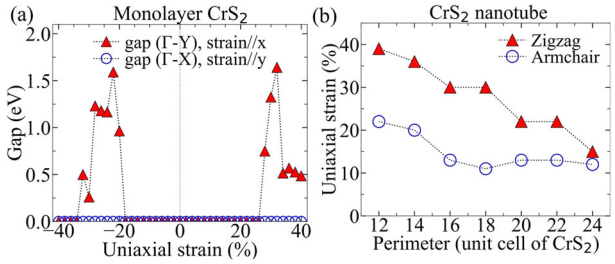

Fig. 5 | Strain-induced band gap changes in monolayer CrS_2 and strain in nanotubes. a Band gap of monolayer CrS_2 along Γ-Y/Γ-X with uniaxial strain along x/y direction. **b** Uniaxial strain along x/y direction of zigzag/armchair CrS_2 nanotubes with different perimeters.

along both directions. Similarly, the band structure and Fermi contour of monolayer CrS_2 under 12% tensile strain along y direction are shown in Fig. 4d, h, respectively.

Extending to nanotubes, zigzag nanotubes experience uniaxial strain along the perimeter, corresponding to the x direction in the monolayer structure (Fig. 4(z1)). As shown in Fig. 4(z2), when the structure transforms from monolayer to 1D zigzag nanotube, the Brillouin zone folds from its 2D planar form into lines parallel to the Γ-Y direction. Fig. 4(z3) show the Fermi contour in the Brillouin zone of monolayer CrS_2, where the 1D Brillouin zone of zigzag nanotube is schematically indicated by lines. The Brillouin zone and the Fermi contour exhibit no intersections, thus demonstrating a semiconducting band structure as shown in Fig. 4(z4).

In contrast, armchair nanotubes experience uniaxial strain along their perimeter, corresponding to y direction in the monolayer structure (Fig. 4(a1)). Upon transformation from monolayer to 1D armchair nanotube, the Brillouin zone folds from a 2D plane into lines parallel to the Γ-X direction. Fig. 4(a3) depicts the Fermi contour for this folded zone, indicated schematically by lines. The presence of intersections between the Fermi contour and the folded zone demonstrates a metallic band structure, as shown in Fig. 4(a4).

The Brillouin zone of zigzag and armchair nanotubes always contains the Γ-Y and Γ-X paths, respectively. The evolution of band gap along Γ-Y/Γ-X line in monolayer CrS_2 under uniaxial strain along x/y direction are presented in Fig. 5a. Without strain, no gap exists along either path; under strain along x direction, a gap opens along Γ-Y for $\epsilon = -32\% \sim -20\%$ and $\epsilon > 28\%$, whereas strain along y direction induces no gap along Γ-X. As depicted in Fig. 5b, the external S atoms experience tensile strain, which decreases from 40% to 15% with increasing nanotube diameter from 14 to 24 CrS_2 units. As Fig. 5a shows, semiconducting behavior in zigzag nanotubes requires a large tensile strain (>28%), limiting it to narrow tubes with big strain. For example, in semiconducting Z-18-CrS_2, outer S, Cr, and inner S layers exhibit large strains of −23%, 13%, and 30%, respectively. The DFT results for TMD nanotubes are not entirely consistent with those from the 2D band structure, primarily due to their complex structure comprising multiple atomic layers subjected to different strains. Together, Brillouin zone folding and uniaxial strain govern the diameter- and configuration-dependent metal-to-semiconductor transition in TMD nanotubes. The strained band structures of monolayer CrS_2 are provided in Supplementary Figs. S1, S2 and Supplementary Material.

Calculation of Curie temperature T_C of the nanotube

To study the magnetic properties of the zigzag CrS_2 nanotube with 18 CrS_2 units (Z-18-CrS_2), we consider a Heisenberg-type Hamiltonian:

$$H = J \sum_{<i,j>} \vec{S_i} \cdot \vec{S_j} + \sum_i A_{\parallel} S_{i\parallel}^2, \tag{2}$$

where $\vec{S_i}$ and $\vec{S_j}$ are spin operators of Cr atoms at site i and j, respectively, J is the exchange coupling constant between the nearest-neighboring Cr atoms. $A_{\parallel}$ is the single-ion magnetic anisotropy parameter defined as $A_{\parallel}S^2 = (E_{\parallel} - E_{\perp})/N_{Cr}$, where $E_{\parallel}$ and $E_{\perp}$ are the DFT results of energies of

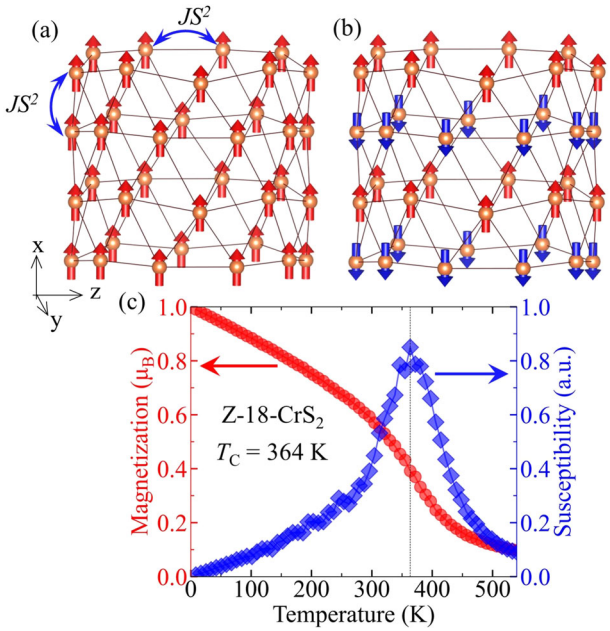

Fig. 6 | Spin configurations and Monte Carlo results of Z-18-CrS_2. A FM (**a**) and an AFM (**b**) spin configuration are considered to get the exchange coupling parameter JS^2. **c** Magnetization and susceptibility of Z-18-CrS_2 as a function of temperature, obtained by the Monte Carlo simulation, giving a T_C of 364 K.

CrS_2 nanotube with magnetization parallel and perpendicular to the extension direction of nanotube, respectively. N_{Cr} is the number of Cr atoms in the considered cell. The calculated result of $A_{\parallel}S^2$ is −0.82 meV/Cr, indicating that the magnetization is parallel to the extension direction of the nanotube. Energies of Z-18-CrS_2 nanotube with an FM and an AFM spin configurations, as shown in Fig. 6a, b, respectively, can be expressed as

$$\begin{aligned} E_{FM} &= 3N_{Cr}JS^2 + E_0, \\ E_{AFM} &= -N_{Cr}JS^2 + E_0. \end{aligned} \tag{3}$$

E_0 is the energy part independent of spin configurations, which is included in the total energy of DFT results for Z-18-CrS_2. N_{Cr} is the number of Cr atoms in the unit cell of the nanotube, i.e., 18 for Z-18-CrS_2. The exchange coupling parameter JS^2 can be calculated by $JS^2 = (E_{FM} - E_{AFM})/(4N_{Cr})$. The DFT results of the relative total energy of Z-18-CrS_2 in FM and AFM states are 0 and 2132.8 meV, respectively, which gives $JS^2 = -29.62$ meV. By the Monte Carlo simulation based on the Heisenberg model in Eq. (3), the temperature-dependent magnetization and susceptibility of Z-18-CrS_2 were calculated, as shown in Fig. 6c, giving a T_C of 364 K.

Due to their similar structures, all nanotubes are calculated in this way. The T_C of zigzag type CrS_2, $CrTe_2$, and VSe_2 nanotubes are obtained, as shown in Fig. 2c. $T_C \sim 300$ K for zigzag CrS_2 nanotubes, ~450 K for zigzag $CrTe_2$ nanotubes and ~100 K for zigzag VSe_2 nanotubes are observed. From monolayer ferromagnetic metals with high T_C to nanotubes, they maintain strong ferromagnetic coupling. The data are presented in Table 1. The T_C in armchair configuration shows similar values of T_C in zigzag configuration.

Among these materials, Z-18-CrS_2 and Z-18-$CrTe_2$ are room temperature ferromagnetic semiconductors, corresponding to diameters of 1.28 nm and 1.45 nm, respectively. Z-18-CrS_2 is an FM semiconductor with T_C of 364 K and a band gap of 0.53 eV. Z-18-$CrTe_2$ shows T_C of 431 K and a band gap of 0.16 eV. To obtain their accurate band gaps, the HSE functional is applied in DFT calculation[111]. Metal-to-semiconductor transition happens in CrS_2 and $CrTe_2$ from monolayer to zigzag nanotubes. E_{strain} of 0.05 eV/atom and 0.09 eV/atom are observed in Z-18-CrS_2 and Z-18-$CrTe_2$, respectively, indicating their feasibility of preparation. Detailed results concerning the band gap, diameter, Curie temperature T_C, and strain energy E_{strain} of zigzag and armchair CrS_2 and $CrTe_2$ nanotubes are summarized in Table 1.

Table 2 | Coupling constants and Curie temperatures for CrS_2 nanotubes and monolayer CrS_2

Perimeter (CrS_2 units)	Coupling constants (meV)			T_C (K) estimated by		$\frac{T_C(J_1,J_2,J_3)}{T_C(J_1)}$
	J_1S^2	J_2S^2	J_3S^2	J_1	J_1,J_2,J_3	
12	− 16.96	− 6.75	4.92	208	230	111%
14	− 11.50	− 8.28	6.61	141	158	112%
16	− 16.89	− 7.78	6.38	207	222	107%
18	− 19.38	− 14.30	10.08	238	309	130%
20	− 14.08	− 11.26	9.57	173	246	142%
22	− 15.38	− 10.95	8.48	189	222	117%
24	− 15.33	− 5.45	6.04	188	151	80%
∞ (monolayer)	− 10.78	− 4.53	− 3.20	132	295	224%

The exchange coupling constants for the first (J_1), second (J_2), and third (J_3) nearest-neighbor interactions for zigzag CrS_2 nanotubes with different perimeters and monolayer CrS_2, obtained by DFT calculations. The T_C obtained by MC simulations. $T_C(J_1, J_2, J_3)$: $T_C(J_1)$ is also listed.

Table 3 | Coupling constants of zigzag CrS_2 nanotubes containing 12 and 18 CrS_2 units, obtained by DFT calculation and Eq. (4)

Perimeter (CrS_2 units)	$J_{DFT}S^2$	$J^{super}A$	$J_{24}^{super}A$
12	− 20.9	11.4	9.9
18	− 29.6	28.1	32.8

The result of superexchange $J_{24}^{super}A$ between Cr_2 and Cr_4 in Fig. 7 is given. The units of $J_{DFT}S^2$ and $J^{super}A$ are meV and eV^3, respectively.

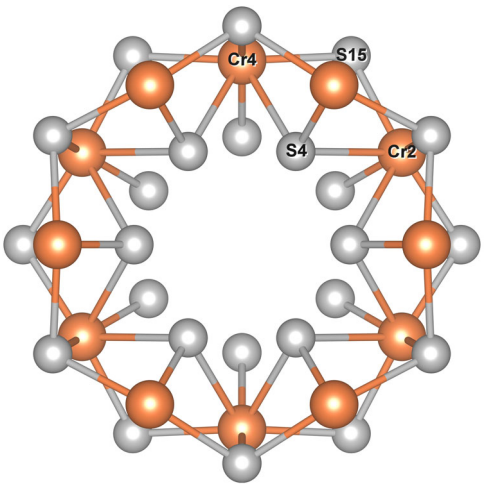

Fig. 7 | Structure of Z-12-CrS_2. The zigzag CrS_2 nanotube with a perimeter of 12 CrS_2 units (Z-12-CrS_2), highlighting the superexchange path between Cr_2 and Cr_4.

Discussion on T_C of monolayer CrS_2 and zigzag CrS_2 nanotubes

The exchange couplings of monolayer CrS_2 and zigzag CrS_2 nanotubes exhibit distinct characteristics. Using DFT calculations, we determined the exchange coupling constants for the first (J_1), second (J_2), and third (J_3) nearest-neighbor interactions, as summarized in Table 2. Detailed calculation process are given in the Method section. For monolayer CrS_2, our DFT results reveal ferromagnetic coupling with $J_1S^2 = -10.78$ meV, $J_2S^2 = -4.53$ meV, and $J_3S^2 = -3.20$ meV. Monte Carlo simulations demonstrate that including only J_1 yields a T_C of 132 K. In contrast, zigzag CrS_2 nanotubes exhibit more complex magnetic interactions. While J_1 remains ferromagnetic and dominant in magnitude, J_2 also favors ferromagnetism while J_3 becomes antiferromagnetic. This competition results in T_C being primarily governed by J_1. For Z-18-CrS_2 nanotubes: $J_1S^2 = -19.38$ meV, $J_2S^2 = -14.30$ meV, and $J_3S^2 = 10.08$ meV. Monte Carlo simulations predict $T_C = 238$ K when considering only J_1, rising to 309 K when all three couplings are included. Similarly, for Z-12-CrS_2 nanotubes: $J_1S^2 = -16.96$ meV, $J_2S^2 = -6.75$ meV, and $J_3S^2 = 4.92$ meV. The

Table 4 | The parameters of superexchange coupling in Eq. (4) for the zigzag CrS_2 nanotubes with perimeters of 12 and 18 CrS_2 units, obtained by DFT

Orbital of Cr	Orbital of S	Perimeter (CrS_2 units)	$\lvert V_{pd}\rvert^2$	$\lvert E_p\text{-}E_d\rvert$	$\frac{\lvert V_{pd}\rvert^4}{\lvert E_p-E_d\rvert}$
Cr_2 $d_{xz}(\uparrow)$	S_4 $p_y(\uparrow)$	12	3.98	0.47	0.055
		18	2.84	0.43	0.064
Cr_2 $d_{z2}(\uparrow)$	S_{15} $p_z(\uparrow)$	12	0.00	2.22	0.000
		18	0.57	1.28	0.255
Cr_2 $d_{z2}(\uparrow)$	S_{15} $p_x(\uparrow)$	12	0.21	2.98	0.015
		18	0.57	1.47	0.244
Cr_2 $d_{xz}(\uparrow)$	S_{15} $p_z(\uparrow)$	12	0.28	2.68	0.040
		18	0.77	1.48	0.417
Cr_4 $d_{z2}(\uparrow)$	S_4 $p_y(\uparrow)$	12	0.07	3.84	0.001
		18	0.87	2.54	0.287
Cr_4 $d_{xz}(\uparrow)$	S_4 $p_z(\uparrow)$	12	0.20	3.76	0.011
		18	1.17	2.59	0.531
Cr_4 $d_{yz}(\uparrow)$	S_{15} $p_z(\uparrow)$	12	0.33	2.21	0.050
		18	0.40	1.52	0.103
Cr_4 $d_{x2-y2}(\uparrow)$	S_{15} $p_x(\uparrow)$	12	0.50	2.87	0.086
		18	0.63	1.66	0.238
Cr_4 $d_{xy}(\uparrow)$	S_{15} $p_y(\uparrow)$	12	0.54	2.30	0.125
		18	0.77	1.34	0.444

Units of $|E_p - E_d|$, $|V_{pd}|^2$, and $|V_{pd}|^4/|E_p - E_d|$ are eV, eV^2, and eV^3, respectively.

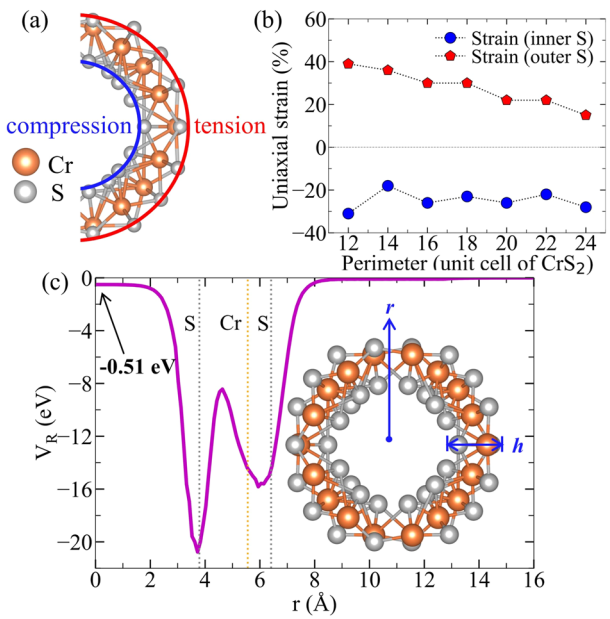

Fig. 8 | Radial polarization driven by radial strain gradient in nanotubes. a Cross-sectional view of a zigzag CrS_2 nanotube showing compressive strain in the inner wall and tensile strain in the outer wall. **b** Dependence of inner and outer wall strain on the nanotube perimeter. **c** The radial electrostatic potential V_R of Z-18-CrS_2. V_R inside of tube is 0.51 eV lower than outside.

Table 5 | For zigzag magnetic nanotubes family MX_2, the band gap, diameter d, Curie temperature T_C, and strain energy E_{strain}

Perimeter	MX_2	Properties				MX_2	Properties				MX_2	Properties			
(MX_2 units)		Gap	T_C	d	E_{strain}		Gap	T_C	d	E_{strain}		Gap	T_C	d	E_{strain}
12		0.32	185.9	0.97	0.28		0.51	43.7	0.97	0.27		0	17.3[A]	1.11	0.09
14		0.77	196.1	1.08	0.17		0.17	78.0	1.07	0.23		0.29	49.9	1.19	0.06
16		0.98	86.3	1.16	0.11		0.68	106.5	1.24	0.08		0.06	44.7	1.30	0.03
18	VS_2	0.24	96.1	1.26	0.08	VSe_2	0	200.4	1.34	0.05	VTe_2	0.21	60.2	1.40	0.01
20		0.16	123.8	1.48	0.08		0	127.9	1.46	0.04		0.01	100.7	1.53	−0.02
22		0.35	124.9	1.61	0.02		0	132.5	1.57	0.00		0	112.2	1.62	−0.01
24		0.68	131.6	1.61	0.02		0.15	141.5	1.69	0.01		0.01	176.8	1.79	−0.03
12		0	233.1	0.92	0.26		0	303.4	0.98	0.22		0	322.3	1.08	0.17
14		0.21	212.7	1.05	0.11		0	430.7	1.09	0.19		0	436.9	1.20	0.14
16		0	267.6	1.14	0.09		0	398.5	1.22	0.12		0	432.4	1.31	0.13
18	CrS_2	0.53*	363.8	1.28	0.05	$CrSe_2$	0	395.5	1.31	0.07	$CrTe_2$	0.16*	431.2	1.45	0.09
20		0	272.8	1.34	0.03		0	425.8	1.40	0.05		0	467.2	1.56	0.06
22		0	280.4	1.46	0.03		0	310.4	1.52	0.03		0	479.0	1.66	0.05
24		0	223.0	1.51	0.01		0	247.2	1.62	0.04		0	477.9	1.77	0.04
12		0	206.7	0.92	0.13		0.74	119.2[A]	0.99	0.09		0.67	100.5[A]	1.11	0.03
14		0.09	233.1	1.08	0.12		0.40	159.9[A]	1.09	0.06		0.32	131.5[A]	1.21	0.05
16		0	262.3	1.20	0.13		0.25	195.2[A]	1.19	0.05		0.28	149.6[A]	1.32	0.03
18	MnS_2	0	473.8	1.33	0.16	$MnSe_2$	0	217.4	1.35	0.03	$MnTe_2$	0	121.9	1.48	0.00
20		0	319.2	1.40	0.10		0	250.0	1.46	0.04		0	200.5	1.61	0.01
22		0	127.5	1.56	0.05		0	223.7	1.58	0.02		0	150.5	1.69	0.01
24		0	240.6	1.56	0.07		0	264.6	1.69	0.02		0	20.9[A]	1.81	0.01
12		0.59	259.4[A]	0.91	0.09		0.42	177.7[A]	0.98	0.12		0.75	264.8	1.21	0.06
14		0.48	193.7[A]	1.01	0.06		0.16	304.4[A]	1.08	0.08		0.49	314.8[A]	1.28	0.00
16		0	90.5[A]	1.18	−0.04		0.19	257.5[A]	1.19	0.06		0	53.3[A]	1.32	0.09
18	FeS_2	0	114.2[A]	1.25	−0.02	$FeSe_2$	0	26.7[A]	1.33	0.04	$FeTe_2$	0	104.0	1.43	0.04
20		0	129.3[A]	1.35	0.00		0	92.3[A]	1.56	0.04		0.24	122.7[A]	1.67	0.01
24		0	291.8[A]	1.60	−0.04		0	181.3[A]	1.69	0.02		0	58.7[A]	18.1	0.04
22		0	352.6[A]	1.47	−0.04		0	251.6[A]	1.56	0.01		0	21.4	1.70	0.03
12		0	270.7[A]	0.98	−0.07		0	164.5[A]	1.11	0.00		0	16.4[A]	1.16	0.02
14		0.21	15.9[A]	1.03	0.07		0	45.5	1.10	0.14		0	194.4[A]	1.16	0.11
16		0.00	31.1	1.11	0.03		0	42.2	1.19	0.08		0	27.9[A]	1.30	0.09
18	CoS_2	0.18	14.3	1.23	−0.01	$CoSe_2$	0	74.6	1.30	0.05	$CoTe_2$	0	186.1[A]	1.39	0.05
20		0	671.7	1.35	−0.04		0	90.4	1.41	0.05		0	76.6[A]	1.49	0.03
22		0	201.6	1.43	−0.04		0	37.8	1.51	0.03		0	25.0[A]	1.61	0.02
24		0	87.2[A]	1.55	−0.03		0	252.1[A]	1.66	0.03		0	84.6[A]	1.75	0.09

Table 5 (continued) | For zigzag magnetic nanotubes family MX_2, the band gap, diameter *d*, Curie temperature T_C, and strain energy E_{strain}

Perimeter	MX_2	Properties				MX_2	Properties				MX_2	Properties			
(MX_2 units)		Gap	T_C	*d*	E_{strain}		Gap	T_C	*d*	E_{strain}		Gap	T_C	*d*	E_{strain}
12		0.79	0.0	1.04	0.08		0	14.9[A]	1.05	0.14		0	0.3	1.09	0.11
14		0.16	23.4	1.00	0.23		0.25	4.3[A]	1.07	0.24		0	0.0	1.17	0.07
16		0	6.3[A]	1.11	0.24		0.23	3.9[A]	1.18	0.19		0	0.0	1.31	0.19
18	NiS_2	0	2.9	1.21	0.20	$NiSe_2$	0.23	0.8[A]	1.29	0.16	$NiTe_2$	0	1.7	1.40	0.15
20		0.25	0.0	1.32	0.16		0.01	2.0[A]	1.40	0.13		0	1.1	1.52	0.13
22		0	24.1[A]	1.40	0.14		0.01	0.0	1.51	0.11		0	0.0	1.63	0.10
24		0.27	10.3[A]	1.52	0.12		0.14	0.0	1.62	0.09		0	9.3	1.76	0.09

The units of *d*, Gap, T_C, and E_{strain} are nm, eV, K, and eV/atom, respectively. The results are obtained by DFT calculations and Monte Carlo simulations. Most band gaps are obtained by the DFT calculation with PBE functional, except the room temperature ferromagnetic semiconductors Z-18-CrS_2 and Z-18-$CrTe_2$ marked by * obtained with HSE functional. The marker of [A] in T_C indicates that the material is antiferromagnetic, and the corresponding value represents the Neel temperature. All structures are obtained by optimization at ferromagnetic ground state.

corresponding T_C values increase from 208 K (J_1 only) to 230 K (all couplings). These findings indicate that while monolayer CrS_2's T_C is determined by the combined effects of J_1, J_2, and J_3, the T_C of zigzag CrS_2 nanotubes is predominantly controlled by the dominant ferromagnetic J_1 interaction.

Since T_C of zigzag CrS_2 nanotubes is predominantly governed by the ferromagnetic J_1 interaction, the observed decrease in T_C with decreasing perimeter can be reasonably attributed to variations in J_1. Recent studies[47,51,112,113] have proposed that ferromagnetic J_1 in two-dimensional magnetic semiconductors and metals can be effectively described by the superexchange model. The superexchange coupling J_{ij}^{super} between Cr atom at site i and Cr atom at site j can be obtained as ref. 51:

$$J_{ij}^{super} = \left(\frac{1}{E_{\uparrow\downarrow}^2} - \frac{1}{E_{\uparrow\uparrow}^2}\right) \sum_{k,p,d} |V_{ik}|^2 J_{kj}^{pd} = \frac{1}{A} \sum_{k,p,d} |V_{ik}|^2 J_{kj}^{pd}. \quad (4)$$

The indirect exchange coupling J_{ij}^{super} consist of two processes. One is the direct exchange process between the *d*-electrons of Cr at site j (Cr_j) and the *p*-electrons of S at site k (S_k), represented by J_{kj}^{pd}. Another is the electron hopping process between the *p*-electrons of S_k and the *d*-electrons of Cr_i, presented by $|V_{ik}|^2/A$. V_{ik} is the hopping parameter between *d* electrons of the Cr_i and *p* electrons of S_k. $A = 1/(1/E_{\uparrow\downarrow}^2 - 1/E_{\uparrow\uparrow}^2)$ is taken as a pending parameter, where $E_{\uparrow\uparrow}$ and $E_{\uparrow\downarrow}$ are energies of two *d* electrons in Cr atoms with parallel and antiparallel spins, respectively. Eq. (4) represents the summation of contributions from all possible superexchange paths between Cr_i and Cr_j via all *p*-orbitals of all intermediate S_k atoms. The direct exchange coupling J_{kj}^{pd} can be expressed as $J_{kj}^{pd} = 2|V_{kj}|^2/|E_k^p - E_j^d|$[47,51,112,113]. V_{kj} is the hopping parameter between *p* electrons of the S_k and *d* electrons of Cr_j, E_k^p is the energy of *p* electrons of the S_k, and E_j^d is the energy of *d* electrons of Cr_j.

The parameters V_{ik}, V_{kj}, E_k^p, and E_j^d in Eq. (4) are obtained from DFT and Wannier function calculations. The exchange term $J_{ij}^{super}A$ is computed by summing over all relevant *p* orbitals at all possible S sites and all *d* orbitals at Cr sites. The parameter $J_{ij}^{super}A$ is an analytical construct, not a fundamental physical observable. Composed of the superexchange constant J_{ij}^{super} (unit: eV) and parameter A (unit: eV^2), its derived dimension is energy cubed (eV^3). This unconventional unit arises mathematically from our deliberate construction: $J_{ij}^{super}A$ serves as a theoretical tool to isolate hopping-dependent trends in superexchange interactions by explicitly factoring out the A term from the exchange coupling framework. The nearest coupling constant $J^{super}S^2$ is obtained by averaging couplings:

$$J^{super}S^2 = \frac{1}{z} \sum_{<i,j>} J_{ij}^{super} S^2, \quad (5)$$

where z is the number of nearest couplings, which is 6 in nanotubes. Table 3 presents the calculated values for zigzag CrS_2 nanotubes with perimeters containing 12 and 18 CrS_2 units, demonstrating an increase in superexchange strength with tube diameter. This trend of $J^{super}A$ is consistent with the $J_{DFT}S^2$ values obtained from DFT, where the same parameter A is taken for nanotubes with different diameters.

As an example, we examine the superexchange coupling between Cr atom at site 2 and Cr atom at site 4 in Z-12-CrS_2 mediated by S atoms at sites 4 and 15. The structure is shown in Fig. 7. The coupling strength $J_{24}^{super}A$ increases from 9.9 to 32.8 eV^3 as the nanotube diameter increases from 12 to 18 CrS_2 units, as shown in Table 3. To understand this behavior, we analyze the 3*d* orbital energies E_d of Cr atom at site 2 and Cr atom at site 4, the 5*p* orbital energy E_p of S atoms at sites 4 and 15, and the hopping matrix element $|V_{pd}|$ between them. The superexchange coupling strength is represented by the factor $|V_{pd}|^4/|E_p\text{-}E_d|$, according to Eq. (4). As shown in Table 4, the energy difference $|E_p\text{-}E_d|$ decreases markedly, and the hopping term $|V_{pd}|^2$ increases with perimeter, resulting in a stronger superexchange coupling.

Table 6 | For armchair magnetic nanotubes family MX_2, the band gap, diameter d, Curie temperature T_C, and strain energy E_{strain}

Perimeter	MX_2	Properties				MX_2	Properties				MX_2	Properties			
(MX_2 units)		Gap	T_C	d	E_{strain}		Gap	T_C	d	E_{strain}		Gap	T_C	d	E_{strain}
12		0	67.8[A]	1.39	0.10		0.11	195.5	1.46	0.05		0.75	197.2	1.59	−0.02
14		0	76.0[A]	1.58	0.07		0	209.1	1.64	0.01		0	156.6	1.79	−0.03
16		0	63.9	1.85	0.05		0	21.0	1.92	0.03		0	78.0	1.98	−0.07
18	VS_2	0	67.8	2.04	0.03	VSe_2	0	24.5	2.12	0.01	VTe_2	0	52.7	2.21	−0.08
20		0	69.7	2.23	0.02		0	17.6	2.32	0.00		0	64.2	2.40	−0.09
22		0	184.8	2.42	0.01		0	15.2	2.53	−0.01		0	455.7	2.61	−0.09
24		0	72.2	2.61	0.01		0	113.9[A]	2.73	−0.01		0	179.8	2.80	−0.09
12		0	285.8	1.38	0.07		0	319.1	1.49	0.10		0	374.8	1.58	0.11
14		0	298.7	1.58	0.05		0	364.2	1.65	0.06		0	441.0	1.78	0.07
16		0	328.5	1.71	0.02		0	367.9	1.81	0.02		0	322.5	1.99	0.04
18	CrS_2	0	274.6	1.88	0.02	$CrSe_2$	0	356.9	1.99	0.01	$CrTe_2$	0	318.1	2.21	0.02
20		0	232.3	2.13	0.02		0	323.6	2.16	0.00		0	309.7	2.40	0.02
22		0	257.6	2.34	0.02		0	308.5	2.35	0.00		0	291.1	2.61	0.02
24		0	246.5	2.52	0.01		0	292.3	2.54	−0.01		0	254.5	2.80	0.01
12		0	136.0	1.44	0.04		0	193.9	1.50	−0.02		0	159.6	1.58	−0.03
14		0	230.0	1.62	0.04		0	228.6	1.68	−0.02		0	204.5	1.81	−0.04
16		0	328.7	1.84	0.07		0	242.2	1.93	0.06		0	54.1	2.01	−0.01
18	MnS_2	0	326.9	2.03	0.06	$MnSe_2$	0	355.6	2.15	0.05	$MnTe_2$	0	207.9	2.25	−0.03
20		0	325.5	2.21	0.05		0	344.6	2.35	0.04		0	1.8[A]	2.41	0.00
22		0	327.4	2.40	0.04		0	356.3	2.55	0.03		0	181.8	2.63	−0.04
24		0.02	325.7	2.59	0.03		0	343.5	2.74	0.03		0	159.3	2.86	−0.02
12		0	154.9[A]	1.41	−0.02		0	79.2[A]	1.47	0.00		0	145.8[A]	1.55	0.01
14		0	278.2[A]	1.58	−0.02		0	148.4[A]	1.65	−0.01		0	405.3 [A]	1.77	0.00
16		0	129.6[A]	1.77	−0.03		0	96.7[A]	1.87	−0.01		0	88.2[A]	2.03	0.00
18	FeS_2	0	134.5[A]	1.96	0.01	$FeSe_2$	0	106.6[A]	2.06	0.01	$FeTe_2$	0	130.7[A]	2.20	0.03
20		0	138.1[A]	2.14	0.00		0	88.2[A]	2.26	0.01		0	117.9[A]	2.38	0.02
22		0	139.5[A]	2.32	0.00		0	79.4[A]	2.46	0.00		0	75.8[A]	2.60	0.03
24		0	139.3[A]	2.51	−0.01		0	77.3[A]	2.64	0.00		0	113.5[A]	2.78	0.02
12		0	177.0[A]	1.39	−0.01		0	31.4[A]	1.43	0.04		0	40.8[A]	1.53	0.09
14		0	262.1[A]	1.56	−0.03		0	205.0[A]	1.61	0.00		0	23.1[A]	1.73	0.06
16		0	207.8[A]	1.73	0.01		0	479.6	1.84	0.11		0	7.0[A]	1.95	0.07
18	CoS_2	0	217.1[A]	1.91	0.00	$CoSe_2$	0	633.6[A]	2.05	0.06	$CoTe_2$	0	0.1	2.15	0.05
20		0	249.7[A]	2.10	0.00		0	647.6[A]	2.25	0.04		0	0.0	2.35	0.04
22		0	221.8[A]	2.28	0.01		0	486.4[A]	2.45	0.05		0	0.0	2.55	0.04
24		0	337.5[A]	2.49	0.01		0	383.4[A]	2.65	0.06		0	0.0	2.75	0.03

Table 6 (continued) | For armchair magnetic nanotubes family MX_2, the band gap, diameter *d*, Curie temperature T_C, and strain energy E_{strain}

Perimeter	MX_2	Properties				MX_2	Properties				MX_2	Properties			
(MX_2 units)		Gap	T_C	*d*	E_{strain}		Gap	T_C	*d*	E_{strain}		Gap	T_C	*d*	E_{strain}
12	NiS_2	0	9.7[A]	1.34	0.18	$NiSe_2$	0	3.0[A]	1.41	0.17	$NiTe_2$	0	15.4	1.49	0.19
14		0	13.6[A]	1.51	0.16		0	24.9[A]	1.59	0.14		0	10.2[A]	1.70	0.15
16		0.35	0.0	1.72	0.08		0	0.0	1.83	0.07		0	1.1	1.97	0.07
18		0.35	0.0	1.90	0.07		0	0.0	2.02	0.06		0	1.8	2.17	0.05
20		0.36	0.0	2.09	0.06		0	0.0	2.21	0.05		0	4.5	2.37	0.05
22		0.38	0.0	2.26	0.05		0	0.0	2.40	0.04		0	4.5	2.57	0.04
24		0.37	0.0	2.45	0.04		0	0.0	2.60	0.03		0	7.0	2.77	0.03

The units of *d*, Gap, T_C, and E_{strain} are nm, eV, K, and eV/atom, respectively. The results are obtained by DFT calculations and Monte Carlo simulations. All band gaps are obtained by the DFT calculation with the PBE functional. The marker of [A] in T_C indicates that the material is antiferromagnetic, and the corresponding value represents the Neel temperature. All structures are obtained by optimization at the ferromagnetic ground state.

Calculation of electric polarization E_r of nanotube

According to previous studies of flexoelectricity, an inhomogeneous strain will break the inversion symmetry of 2D materials, and electric polarization is permitted[114–116]. Flexoelectricity holds immense application potential in sensors, actuators, and next-generation electronic devices[117–119], which has been reported to tune magnetic properties in some materials[120,121]. When a nanotube is formed by rolling a 2D layer of finite thickness, radial electric polarization is possible due to the difference in strain between the inside and outside of the wall[105,106]. We calculated the flexoelectric-like radial polarization of nanotubes. The radial electrostatic polarization is obtained by $E_r = (V_R(outside) - V_R(inside))/h$, where $V_R(inside)$ and $V_R(outside)$ are the radial electrostatic potential inside and outside of the nanotube, and h is the thickness of the tube wall[105]. The radial electrostatic potential $V_R(r)$ is obtained by converting the DFT results of electrostatic potential $V(r, \theta, z)$ to a function of radius by $V_R(r) = \int d\theta \int V(r, \theta, z)/(2\pi z_0) dz$, where r, θ, and z are the three parameters of position in cylindrical coordinates, and z_0 is the length of unit cell. The radial electrostatic potential of Z-18-CrS_2 outside of tube is 0.51 eV higher than inside, as shown in Fig. 8c. Considering a thickness h of 2.6 Å, the effective electrical polarization is 0.19 eV/Å inward along the radius. All electrical polarization of nanotubes was obtained in similar way. As shown in Fig. 2d), E_r of nanotubes decreases with increasing diameters. The data are presented in Table 1. Both zigzag and armchair nanotubes show radial electrical polarization at 0.1 eV/Å level inward along the radius.

The radial polarization correlates positively with the strain difference between the inner and outer layers of the nanotube (Fig. 8a). As the tube circumference expands from 12 to 24 CrS_2 units, the outer layer relaxes from 40 % to 15 % strain while the inner layer holds at −25% (Fig. 8b), diminishing the overall strain differential and reducing polarization. The geometric parameters also dominate the Curie temperature (Fig. 2c). Because both E_r and T_C derive from nanotube geometry, independent adjustment of each one and analyzing their direct coupling is challenging.

The properties of zigzag and armchair magnetic nanotubes family MX_2

In a similar way, MX_2 nanotubes (M = V, Cr, Mn, Fe, Co, Ni; X = S, Se, Te) nanotubes were calculated in a similar way. Some high T_C ferromagnetic semiconductors are predicted, such as Z-12-$FeTe_2$ and A-12-VTe_2 with T_C higher than 200 K. They show E_{strain} lower than 0.06 eV/atom, indicating their stability. The detailed results of zigzag nanotubes and armchair nanotubes are shown in Tables 5 and 6, respectively.

Discussion

By rolling the 2D high T_C ferromagnetic metals MX_2 (M = V, Cr, Mn, Fe, Co, Ni; X = S, Se, Te) into nanotubes, we theoretically predicted some high T_C ferromagnetic semiconductors, including Z-18-CrS_2 with T_C of 364 K and band gap of 0.53 eV, Z-18-$CrTe_2$ with T_C of 441 K and band gap of 0.16 eV. The predicted nanotubes show strain energies lower than experimental nanotubes, such as narrow CNTs and BN nanotubes, suggesting the feasibility of preparation. In addition, an electrical polarization on the order of 0.1 eV/Å inward of the radial direction is observed due to the strain gradient in the tube wall. Our theoretical results demonstrate a way to obtain high T_C ferromagnetic semiconducting nanotubes derived from experimentally obtained 2D high T_C ferromagnetic metals.

Methods

Density functional theory calculations

All calculations were based on the DFT as implemented in the Vienna ab initio simulation package (VASP)[122]. The exchange-correlation potential is described by the Perdew-Burke-Ernzerhof (PBE) form with the generalized gradient approximation (GGA)[123]. The electron-ion potential is described by the projector-augmented wave (PAW) method[124]. We carried out the calculation of PBE + U with U = 4 eV for 3d elements. The band structures were calculated in Heyd-Scuseria-Ernzerhof (HSE) hybrid functional[111]. The plane-wave cutoff energy is set to be 600 eV. 7 × 1 × 1 Γ center K-points were used for the Brillouin zone (BZ) sampling in nanotubes. The structures of all

materialÅ, respectively. The Wannier90 code was used to construct a tight-binding Hamiltonian[125,126] to calculate the magnetic coupling constants.

Monte Carlo program

The Heisenberg-type Monte Carlo simulation of monolayer CrS_2 and Z-18-CrS_2 nanotubes was performed on $25\times25\times1$ and $50\times1\times1$ lattices, respectively. 1×10^5 steps were carried out for each temperature, and the last one-thirds steps were used to calculate the temperature-dependent physical quantities. The Curie temperature calculation algorithm has been validated in previous work on some 2D and 3D ferromagnetic and antiferromagnetic systems, as shown in Table 7. Results of monolayers $MnSe_2$[39,127], $CrTe_2$[29], Cr_3Te_6[31,51], $Cr_2Ge_2Te_6$[21,128] and CrS_2[40], and bulk $LaFeO_3$[129,130] are listed. The computed T_C and T_N agree well with experimental measurements, confirming the validity of our calculation.

Calculation of J_1, J_2, J_3 and Curie temperatures of monolayer CrS_2 and monolayer $CrTe_2$

To study the magnetic properties of monolayer CrS_2, we consider the Heisenberg-type Hamiltonian:

$$H = J_1\sum_{\langle i,j\rangle}\vec{S_i}\cdot\vec{S_j}+J_2\sum_{\langle\langle i,j\rangle\rangle}\vec{S_i}\cdot\vec{S_j}+J_3\sum_{\langle\langle\langle i,j\rangle\rangle\rangle}\vec{S_i}\cdot\vec{S_j}+A\sum_i S_{iz}^2+E_0, \quad (6)$$

Table 7 | Comparison between calculated and experimental T_C and T_N values for some 2D and 3D magnetic materials

Material	Calculated T_C	Experiments
ML-$MnSe_2$ (metal)	354 K[127]	>300 K[39]
ML-Cr_3Te_6 (metal)	328 K[51]	344 K[31]
ML-$Cr_2Ge_2Te_6$ (semi.)	28 K[128]	30 K (BL)[21]
Bulk $LaFeO_3$ (semi.)	650 K(T_N)[130]	740 K(T_N)[129]
ML-CrS_2 (metal)	295 K	>300 K[40]
ML-$CrTe_2$ (metal)	352 K	>320 K(T_N)[29]

where $\vec{S_i}$ and $\vec{S_j}$ are spin operators of Cr atoms at sites i and j, respectively. J_1, J_2, and J_3 are the nearest, second-nearest, and third-nearest exchange coupling constants between Cr atoms, as shown in Fig. 9a. A is the single-ion magnetic anisotropy parameter defined as $A=(E_\perp-E_\parallel)/N_{Cr}$, where $E_\perp$ and $E_\parallel$ are energies of monolayer CrS_2 with out-of-plane and in-plane magnetization, respectively. N_{Cr} is the number of Cr atoms in the considered cell. The results are $A=-0.23$ meV/Cr. Energies of monolayer CrS_2 with a ferromagnetic and three antiferromagnetic spin configurations, as shown in Fig. 9a–d, respectively, can be expressed as

$$\begin{aligned} E_{FM} &= 24J_1S^2+24J_2S^2+24J_3S^2+E_0,\\ E_{AFM1} &= 8J_1S^2-8J_2S^2-8J_3S^2+E_0,\\ E_{AFM2} &= -8J_1S^2-8J_2S^2+24J_3S^2+E_0,\\ E_{AFM3} &= -8J_1S^2+8J_2S^2-8J_3S^2+E_0. \end{aligned} \quad (7)$$

E_0 is the energy part independent of spin configurations, which is included in the total energy of DFT results for monolayer CrS_2. The exchange coupling parameters can be calculated by solving the equations. The DFT results of the relative total energy of monolayer CrS_2 in FM, AFM1, AFM2, and AFM3 states are 0, 423, 490, and 520 meV, respectively, which gives $J_1S^2=-10.78$ meV, $J_2S^2=-4.53$ meV and $J_3S^2=-3.20$ meV. HSE hybrid functional approach was used to obtain the energies with different magnetic configurations[111]. $7\times4\times1$ Γ center K-points were used. As shown in Fig. 9e, the Monte Carlo simulation result gives T_C of 295 K, close to the experimental results of $T_C=300$ K[40].

The magnetic properties of monolayer $CrTe_2$ were calculated in a similar way. The lattice constant of monolayer $CrTe_2$ is chosen as the experimental value of $a=b/\sqrt{3}=6.8$ Å[29]. The relative energies of FM, AFM1, AFM2, and AFM3 states are 1350.15, 490.65, 705.26, and 0.00 meV, respectively, showing an AFM3 ground state, agree with previous experiment[29] and DFT studies[131]. The results of coupling constants and MAE are $J_1S^2=24.41$ meV, $J_2S^2=-5.26$ meV, $J_3S^2=19.41$ meV, and $A=-3.00$ meV/Cr, respectively. As shown in Fig. 9f, the Monte Carlo simulation result gives T_N of 352 K, which agrees with the experimental results above room temperature[29].

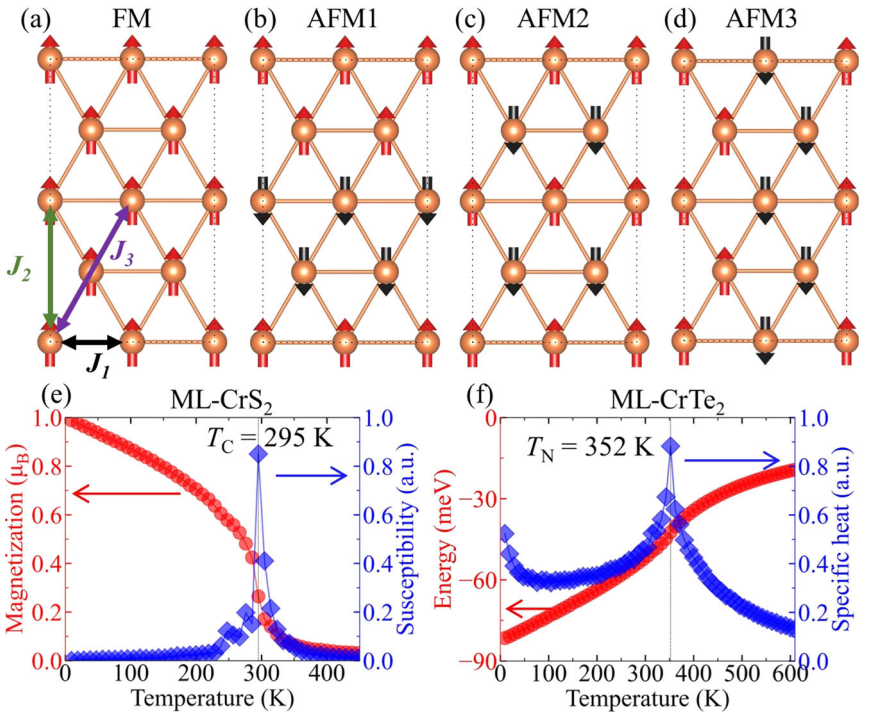

Fig. 9 | Spin configurations and Monte Carlo results of monolayers CrS_2 and $CrTe_2$. A ferromagnetic (FM) (**a**) and three antiferromagnetic (AFM) (**b**–**d**) spin configurations are considered to get the exchange coupling parameters. **e** The magnetization and susceptibility of monolayer CrS_2 as a function of temperature obtained by the Monte Carlo simulation, give a T_C of 295 K. **f** The energy and specific heat of monolayer $CrTe_2$ as a function of temperature obtained by the Monte Carlo simulation, give a T_N of 352 K.

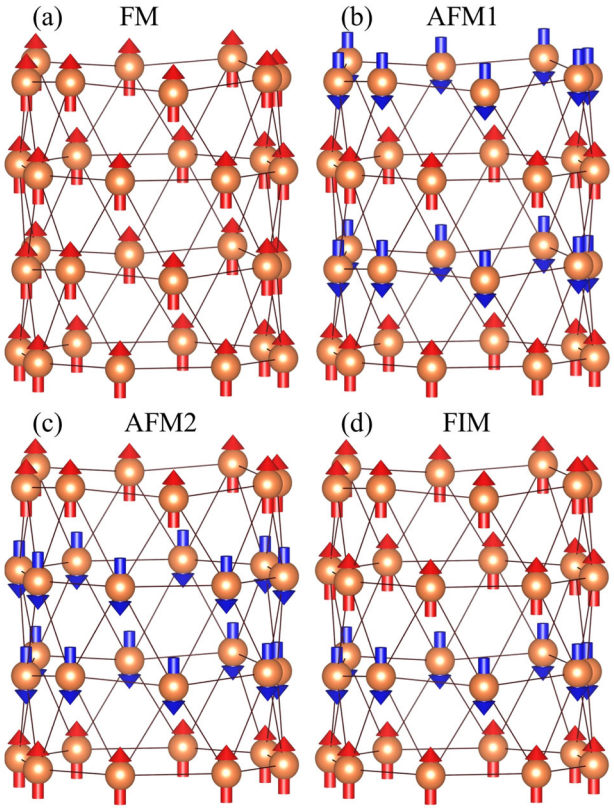

Fig. 10 | Spin configurations considered for CrS_2 nanotubes. A ferromagnetic (FM) (**a**), two antiferromagnetic (AFM) (**b**, **c**), and one ferrimagnetic (FIM) (**d**) spin configurations are considered to get the exchange coupling parameters.

Calculation of J_1, J_2 and J_3 for Zigzag CrS_2 nanotubes

To calculate the magnetic coupling constants of zigzag CrS_2 nanotubes, we consider the Heisenberg-type Hamiltonian similar to Eq. (6). One FM, two AFM, and a ferrimagnetic configuration are considered, as shown in Fig. 10a–d, respectively. Their energies can be expressed as

$$\begin{aligned} E_{\mathrm{FM}}/N_{\mathrm{Cr}} &= 12J_1S^2 + 12J_2S^2 + 12J_3S^2 + E_0/N_{\mathrm{Cr}}, \\ E_{\mathrm{AFM1}}/N_{\mathrm{Cr}} &= -2J_1S^2 - 2J_2S^2 + 12J_3S^2 + E_0/N_{\mathrm{Cr}}, \\ E_{\mathrm{AFM2}}/N_{\mathrm{Cr}} &= 2J_1S^2 - 2J_2S^2 - 2J_3S^2 + E_0/N_{\mathrm{Cr}}, \\ E_{\mathrm{AFM3}}/N_{\mathrm{Cr}} &= 4J_1S^2 + 4J_3S^2 + E_0/N_{\mathrm{Cr}}. \end{aligned} \tag{8}$$

N_{Cr} is the number of Cr atoms in the considered cell. The DFT results of the relative total energy of Z-18-CrS_2 in FM, AFM1, AFM2, and FIM states are −582.22 meV, −577.98, −579.94 meV, and −580.01 meV, respectively. The calculated coupling constants are $J_1S^2 = -19.38$ meV, $J_2S^2 = -14.30$ meV, and $J_3S^2 = 10.08$ meV, respectively.

Data availability

The data supporting the findings of this paper are available from the corresponding authors upon reasonable request.

Received: 5 February 2025; Accepted: 12 July 2025;
Published online: 24 September 2025

References

1. Dietl, T. A ten-year perspective on dilute magnetic semiconductors and oxides. *Nat. Mater.* **9**, 965 (2010).
2. Ohno, H. A window on the future of spintronics. *Nat. Mater.* **9**, 952 (2010).
3. Sato, K. et al. Zeller, First-principles theory of dilute magnetic semiconductors. *Rev. Mod. Phys.* **82**, 1633 (2010).
4. Jungwirth, T., Sinova, J., Mašek, J., Kučera, J. & MacDonald, A. H. Theory of ferromagnetic (III, Mn) V semiconductors. *Rev. Mod. Phys.* **78**, 809 (2006).
5. Dietl, T. & Ohno, H. Dilute ferromagnetic semiconductors: physics and spintronic structures. *Rev. Mod. Phys.* **86**, 187 (2014).
6. Ohno, H. Making nonmagnetic semiconductors ferromagnetic. *Science* **281**, 951 (1998).
7. Kalita, H., Bhushan, M. & Singh, L. R. A comprehensive review on theoretical concepts, types and applications of magnetic semiconductors. *Mater. Sci. Eng. B: Solid-State Mater. Adv. Technol.* **288**, 116201 (2023).
8. Fang, M. & Yang, E.-H. Advances in two-dimensional magnetic semiconductors via substitutional doping of transition metal dichalcogenides. *Materials* **16**, 3701 (2023).
9. Telegin, A. & Sukhorukov, Y. Magnetic semiconductors as materials for spintronics. *Magnetochemistry* **8**, 173 (2022).
10. Holub, M., Shin, J., Chakrabarti, S. & Bhattacharya, P. Electrically injected spin-polarized vertical-cavity surface-emitting lasers. *Appl. Phys. Lett.* **87**, 091108 (2005).
11. Fiederling, R. et al. Injection and detection of a spin-polarized current in a light-emitting diode. *Nature* **402**, 787 (1999).
12. Ohno, H. et al. Electric-field control of ferromagnetism. *Nature* **408**, 944 (2000).
13. Mitra, C. et al. p-n diode with hole- and electron-doped lanthanum manganites. *Appl. Phys. Lett.* **79**, 2408 (2001).
14. Bebenin, N. & Ustinov, V. Inverse spin population near ferromagnet/nonmagnetic semiconductor contact. *J. Magn. Magn. Mater.* **272-276**, 1917 (2004).
15. Li, X. et al. Spin-dependent transport in van der Waals magnetic tunnel junctions with Fe_3GeTe_2 electrodes. *Nano Lett.* **19**, 5133 (2019).
16. Song, T. et al. Giant tunneling magnetoresistance in spin-filter van der Waals heterostructures. *Science* **360**, 1214 (2018).
17. Gorbenko, O., Loshkareva, N. & Mostovshchikova, E. Synthetic routes to colossal magnetoresistance manganites thin films containing unstable or highly volatile metal oxides. *Thin Solid Films* **515**, 6395 (2007).
18. Goel, S. et al. Room-temperature spin injection from a ferromagnetic semiconductor. *Sci. Rep.* **13**, 2181 (2023).
19. Cinchetti, M. et al. Determination of spin injection and transport in a ferromagnet/organic semiconductor heterojunction by two-photon photoemission. *Nat. Mater.* **8**, 115 (2008).
20. Huang, B. et al. Layer-dependent ferromagnetism in a van der Waals crystal down to the monolayer limit. *Nature* **546**, 270 (2017).
21. Gong, C. et al. Discovery of intrinsic ferromagnetism in two-dimensional van der Waals crystals. *Nature* **546**, 265 (2017).
22. Mermin, N. D. & Wagner, H. Absence of ferromagnetism or antiferromagnetism in one- or two-dimensional isotropic Heisenberg models. *Phys. Rev. Lett.* **17**, 1307 (1966).
23. Chu, J. et al. Sub-millimeter-scale growth of one-unit-cell-thick ferrimagnetic Cr_2S_3 nanosheets. *Nano Lett.* **19**, 2154 (2019).
24. Cai, X. et al. Atomically thin $CrCl_3$: an in-plane layered antiferromagnetic insulator. *Nano Lett.* **19**, 3993 (2019).
25. Zhang, Z. et al. Direct photoluminescence probing of ferromagnetism in monolayer two-dimensional $CrBr_3$. *Nano Lett.* **19**, 3138 (2019).
26. Achinuq, B. et al. Covalent mixing in the 2D ferromagnet $CrSiTe_3$ evidenced by magnetic X-ray circular dichroism. *Phys. Status Solidi* **16**, 2100566 (2021).
27. Lee, K. et al. Magnetic order and symmetry in the 2D semiconductor CrSBr. *Nano Lett.* **21**, 3511 (2021).
28. Zhang, X. et al. Room-temperature intrinsic ferromagnetism in epitaxial $CrTe_2$ ultrathin films. *Nat. Commun.* **12**, 2492 (2021).

29. Xian, J.-J. et al. Spin mapping of intralayer antiferromagnetism and field-induced spin reorientation in monolayer $CrTe_2$. *Nat. Commun.* **13**, 13:257 (2022).
30. Wang, D. et al. Strain- and electron doping-induced in-plane spin orientation at room temperature in single-layer $CrTe_2$. *ACS Appl. Mater. Interfaces* **16**, 28791–28797 (2024).
31. Chua, R. et al. Room temperature ferromagnetism of monolayer chromium telluride with perpendicular magnetic anisotropy. *Adv. Mater.* **33**, 2103360 (2021).
32. Li, B. et al. Air-stable ultrathin Cr_3Te_4 nanosheets with thickness-dependent magnetic biskyrmions. *Mater. Today* **57**, 66 (2022).
33. Zhang, Y. et al. Ultrathin magnetic 2D single–crystal CrSe. *Adv. Mater.* **31**, 1900056 (2019).
34. Deng, Y. et al. Gate-tunable room-temperature ferromagnetism in two-dimensional Fe_3GeTe_2. *Nature* **563**, 94 (2018).
35. Fei, Z. et al. Two-dimensional itinerant ferromagnetism in atomically thin Fe_3GeTe_2. *Nat. Mater.* **17**, 778 (2018).
36. Seo, J. et al. Nearly room temperature ferromagnetism in a magnetic metal-rich van der Waals metal. *Sci. Adv.* **6**, eaay8912 (2020).
37. Zhang, G. et al. Above-room-temperature strong intrinsic ferromagnetism in 2D van der Waals Fe_3GaTe_2 with large perpendicular magnetic anisotropy. *Nat. Commun.* **13**, 5067 (2022).
38. Chen, Z., Yang, Y., Ying, T. & Guo, J.-g. High-T_c ferromagnetic semiconductor in thinned 3D Ising ferromagnetic metal Fe_3GaTe_2. *Nano Lett.* **24**, 993 (2024).
39. O'hara, D. et al. Room temperature intrinsic ferromagnetism in ewpitaxial manganese selenide films in the monolayer limit. *Nano Lett.* **18**, 3125 (2018).
40. Xiao, H. et al. Van der Waals epitaxial growth of 2D layered room–temperature ferromagnetic CrS_2. *Adv. Mater. Interfaces* **9**, 2201353 (2022).
41. Yao, Y. et al. Synthesis of air-stable 1T-CrS_2 thin films and their application in high-performance floating-gate memory. *J. Mater. Chem. C.* **12**, 11513 (2024).
42. Bonilla, M. et al. Strong room-temperature ferromagnetism in VSe_2 monolayers on van der Waals substrates. *Nat. Nanotechnol.* **13**, 289 (2018).
43. Meng, L. et al. Anomalous thickness dependence of Curie temperature in air-stable two-dimensional ferromagnetic 1T-$CrTe_2$ grown by chemical vapor deposition. *Nat. Commun.* **12**, 94 (2021).
44. You, J.-Y., Dong, X.-J., Gu, B. & Su, G. Possible room-temperature ferromagnetic semiconductors. *Chin. Phys. Lett.* **40**, 067502 (2023).
45. Dong, X.-J., You, J.-Y., Gu, B. & Su, G. Strain-induced room-temperature ferromagnetic semiconductors with large anomalous Hall conductivity in two-dimensional $Cr_2Ge_2Se_6$. *Phys. Rev. Appl.* **12**, 014020 (2019).
46. You, J.-Y., Zhang, Z., Gu, B. & Su, G. Two-dimensional room-temperature ferromagnetic semiconductors with Quantum anomalous Hall effect. *Phys. Rev. Appl.* **12**, 024063 (2019).
47. You, J.-Y., Zhang, Z., Dong, X.-J., Gu, B. & Su, G. Two-dimensional magnetic semiconductors with room curie temperatures. *Phys. Rev. Res.* **2**, 013002 (2020).
48. Huang, C. et al. Ultra-high-temperature ferromagnetism in intrinsic tetrahedral semiconductors. *JACS* **141**, 12413 (2019).
49. Jiang, Z., Wang, P., Xing, J., Jiang, X. & Zhao, J. Screening and design of novel 2D ferromagnetic materials with high Curie temperature above room temperature. *ACS Appl. Mater. Interfaces* **10**, 39032 (2018).
50. Huang, C. et al. Toward intrinsic room-temperature ferromagnetism in two-dimensional semiconductors. *JACS* **140**, 11519 (2018).
51. Li, J.-W., Zhang, Z., You, J.-Y., Gu, B. & Su, G. Two-dimensional Heisenberg model with material-dependent superexchange interactions. *Phys. Rev. B.* **107**, 224411 (2023).
52. Chen, S. et al. Prediction of room-temperature ferromagnetism in a two-dimensional direct band gap semiconductor. *Nanoscale* **12**, 15670 (2020).
53. Song, G. et al. Intrinsic room-temperature ferromagnetic semiconductor $InCrTe_3$ monolayers with large magnetic anisotropy and large piezoelectricity. *Appl. Phys. Lett.* **118**, 123102 (2021).
54. Iijima, S. Helical microtubules of graphitic carbon. *Nature* **354**, 56 (1991).
55. Wang, X., He, M. & Ding, F. Chirality-controlled synthesis of single-walled carbon nanotubes–from mechanistic studies toward experimental realization. *Mater. Today* **21**, 845 (2018).
56. Dresselhaus, M. S., Dresselhaus, G. and Eklund, P. C. *Science of fullerenes and carbon nanotubes: their properties and applications* (Elsevier, 1996).
57. Hayashi, T. et al. Smallest freestanding single-walled carbon nanotube. *Nano Lett.* **3**, 887 (2003).
58. Guan, L., Suenaga, K. & Iijima, S. Smallest carbon nanotube assigned with atomic resolution accuracy. *Nano Lett.* **8**, 459 (2008).
59. Zheng, L. X. et al. Ultralong single-wall carbon nanotubes. *Nat. Mater.* **3**, 673 (2004).
60. Pan, Z. W. et al. Very long carbon nanotubes. *Nature* **394**, 631 (1998).
61. Xu, T. et al. Creating the smallest bn nanotube from bilayer h–bn. *Adv. Funct. Mater.* **27**, 1603897 (2016).
62. Venkataraman, A., Amadi, E. V., Chen, Y. & Papadopoulos, C. Carbon nanotube assembly and integration for applications. *Nanoscale Res. Lett.* **14**, 220 (2019).
63. Zhang, M. & Li, J. Carbon nanotube in different shapes. *Mater. Today* **12**, 12 (2009).
64. Schroeder, V., Savagatrup, S., He, M., Lin, S. & Swager, T. M. Carbon nanotube chemical sensors. *Chem. Rev.* **119**, 599 (2018).
65. Anzar, N., Hasan, R., Tyagi, M., Yadav, N. & Narang, J. Carbon nanotube - a review on synthesis, properties and plethora of applications in the field of biomedical science. *Sens. Int.* **1**, 100003 (2020).
66. Comparetti, E. J., Pedrosa, Vd. A. & Kaneno, R. Carbon nanotube as a tool for fighting cancer. *Bioconjugate Chem.* **29**, 709 (2017).
67. Raphey, V. et al. Advanced biomedical applications of carbon nanotube. *Mater. Sci. Eng. C.* **100**, 616 (2019).
68. Peng, L.-M., Zhang, Z. & Qiu, C. Carbon nanotube digital electronics. *Nat. Electron.* **2**, 499 (2019).
69. Ates, M., Eker, A. A. & Eker, B. Carbon nanotube-based nanocomposites and their applications. *J. Adhes. Sci. Technol.* **31**, 1977 (2017).
70. Kumanek, B. & Janas, D. Thermal conductivity of carbon nanotube networks: a review. *J. Mater. Sci.* **54**, 7397 (2019).
71. Yang, N., Chen, X., Ren, T., Zhang, P. & Yang, D. Carbon nanotube based biosensors. *Sens. Actuators, B.* **207**, 690 (2015).
72. Chen, K. et al. Printed carbon nanotube electronics and sensor systems. *Adv. Mater.* **28**, 4397 (2016).
73. Eivazzadeh-Keihan, R. et al. Applications of carbon-based conductive nanomaterials in biosensors. *Chem. Eng. J.* **442**, 136183 (2022).
74. Han, X. et al. Structural and magnetic properties of various ferromagnetic nanotubes. *Adv. Mater.* **21**, 4619 (2009).
75. Korneva, G. et al. Carbon nanotubes loaded with magnetic particles. *Nano Lett.* **5**, 879 (2005).
76. Lee, D., Cohen, R. E. & Rubner, M. F. Heterostructured magnetic nanotubes. *Langmuir* **23**, 123 (2006).
77. Son, S. J., Reichel, J., He, B., Schuchman, M. & Lee, S. B. Magnetic nanotubes for magnetic-field-assisted bioseparation, biointeraction, and drug delivery. *JACS* **127**, 7316 (2005).
78. Guo, J. et al. Recent advances in magnetic carbon nanotubes: synthesis, challenges and highlighted applications. *J. Mater. Chem. B.* **9**, 9076 (2021).

79. Giordano, M. C., Hamdi, M., Mucchietto, A. & Grundler, D. Confined spin waves in magnetochiral nanotubes with axial and circumferential magnetization. *Phys. Rev. Mater.* **7**, 024405 (2023).
80. Shpaisman, N. et al. Controlled synthesis of ferromagnetic semiconducting silicon nanotubes. *J. Phys. Chem. C.* **116**, 8000 (2012).
81. Yan, M., Andreas, C., Kákay, A., García-Sánchez, F. & Hertel, R. Chiral symmetry breaking and pair-creation mediated walker breakdown in magnetic nanotubes. *Appl. Phys. Lett.* **100**, 252401 (2012).
82. Yang, J. et al. Vortex-chirality-dependent standing spin-wave modes in soft magnetic nanotubes. *J. Appl. Phys.* **123**, 033901 (2018).
83. Körber, L. et al. Curvilinear spin-wave dynamics beyond the thin-shell approximation: Magnetic nanotubes as a case study. *Phys. Rev. B.* **106**, 014405 (2022).
84. Gallardo, R., Alvarado-Seguel, P. & Landeros, P. Unidirectional chiral magnonics in cylindrical synthetic antiferromagnets. *Phys. Rev. Appl.* **18**, 054044 (2022).
85. Otálora, J. A., Yan, M., Schultheiss, H., Hertel, R. & Kákay, A. Curvature-induced asymmetric spin-wave dispersion. *Phys. Rev. Lett.* **117**, 227203 (2016).
86. Rüffer, D. et al. Magnetic states of an individual ni nanotube probed by anisotropic magnetoresistance. *Nanoscale* **4**, 4989 (2012).
87. Aftab, S., Iqbal, M. Z. & Rim, Y. S. Recent advances in rolling 2D TMDs nanosheets into 1D TMDs nanotubes/nanoscrolls. *Small* **19**, 2205418 (2022).
88. Shubina, T. V. et al. Excitonic emission in van der Waals nanotubes of transition metal dichalcogenides. *Ann. Phys.* **531**, 1800415 (2019).
89. Gao, Y. & Xu, B. On the generalized thermal conductance characterizations of mixed one-dimensional-two-dimensional van der waals heterostructures and their implication for pressure sensors. *ACS Appl. Mater. Interfaces* **10**, 14221 (2018).
90. Nakanishi, Y. et al. Structural diversity of single–walled transition metal dichalcogenide nanotubes grown via template reaction. *Adv. Mater.* **35**, 2306631 (2023).
91. Kamaei, S. et al. An experimental study on mixed-dimensional 1D-2D van der waals single-walled carbon nanotube-WSe2 hetero-junction. *IEEE Electron Device Lett.* **41**, 645 (2020).
92. Qin, F. et al. Superconductivity in a chiral nanotube. *Nat. Commun.* **8**, 14465 (2017).
93. Qin, F. et al. Diameter-dependent superconductivity in individual WS_2 nanotubes. *Nano Lett.* **18**, 6789 (2018).
94. Zhang, Y. J. et al. Enhanced intrinsic photovoltaic effect in tungsten disulfide nanotubes. *Nature* **570**, 349 (2019).
95. Li, L. et al. A general method for the chemical synthesis of large–scale, seamless transition metal dichalcogenide electronics. *Adv. Mater.* **30**, 1706215 (2018).
96. Kim, B., Park, N. & Kim, J. Giant bulk photovoltaic effect driven by the wall-to-wall charge shift in WS_2 nanotubes. *Nat. Commun.* **13**, 3237 (2022).
97. Xiang, R. et al. One-dimensional van der waals heterostructures. *Science* **367**, 537 (2020).
98. Evarestov, R. A., Bandura, A. V., Porsev, V. V. & Kovalenko, A. V. Phonon spectra, electronic, and thermodynamic properties of WS_2 nanotubes. *J. Comput. Chem.* **38**, 2581 (2017).
99. Zhao, W., Li, Y., Duan, W. & Ding, F. Ultra-stable small diameter hybrid transition metal dichalcogenide nanotubes X-M-Y (X, Y = S, Se, Te; M = Mo, W, Nb, Ta): a computational study. *Nanoscale* **7**, 13586 (2015).
100. Bölle, F. T., Mikkelsen, A. E. G., Thygesen, K. S., Vegge, T. & Castelli, I. E. Structural and chemical mechanisms governing stability of inorganic Janus nanotubes. *npj Comput. Mater.* **7**, 41 (2021).
101. Edström, A., Amoroso, D., Picozzi, S., Barone, P. & Stengel, M. Curved magnetism in CrI_3. *Phys. Rev. Lett.* **128**, 177202 (2022).
102. Bhardwaj, A., Sharma, A. & Suryanarayana, P. Torsional strain engineering of transition metal dichalcogenide nanotubes: an ab initio study. *Nanotechnology* **32**, 47LT01 (2021).
103. Zibouche, N., Philipsen, P. & Kuc, A. Strong variation of electronic properties of MoS_2 and WS_2 nanotubes in the presence of external electric fields. *J. Phys. Chem. C.* **123**, 3892 (2019).
104. Li, F., Tu, K. & Chen, Z. Versatile electronic properties of VSe_2 bulk, few-layers, monolayer, nanoribbons, and nanotubes: a computational exploration. *J. Phys. Chem. C.* **118**, 21264 (2014).
105. Bennett, D. Flexoelectric-like radial polarization of single-walled nanotubes from first-principles. *Electron. Struct.* **3**, 015001 (2021).
106. Dong, J., Hu, H., Li, H. & Ouyang, G. Spontaneous flexoelectricity and band engineering in MS_2 (M = Mo, W) nanotubes. *Phys. Chem. Chem. Phys.* **23**, 20574 (2021).
107. Jalil, A., Sun, Z., Wang, D. & Wu, X. Magnetic and electronic properties of single-walled Mo_2C nanotube: a first-principles study. *J. Phys. Condens. Matter* **30**, 155305 (2018).
108. Chen, K. et al. Diverse electronic and magnetic properties of CrS_2 enabling strain-controlled 2D lateral heterostructure spintronic devices. *npj Comput. Mater.* **7**, 79 (2021).
109. Blase, X., Rubio, A., Louie, S. G. & Cohen, M. L. Stability and band gap constancy of boron nitride nanotubes. *Europhys. Lett.* **28**, 335 (1994).
110. Fathi, D. A review of electronic band structure of graphene and carbon nanotubes using tight binding. *J. Nanotechnol.* **2011**, 1 (2011).
111. Heyd, J., Scuseria, G. E. & Ernzerhof, M. Hybrid functionals based on a screened Coulomb potential. *J. Chem. Phys.* **118**, 8207 (2003).
112. Zhang, Z., You, J.-Y., Gu, B. & Su, G. Antiferromagnetic and electric polarized states in two-dimensional janus semiconductor $Fe_2Cl_3i_3$. *J. Phys. Chem. C.* **124**, 19219 (2020).
113. O'Neill, A. et al. Enhanced room temperature ferromagnetism in highly strained 2D semiconductor $Cr_2Ge_2Te_6$. *ACS Nano* **17**, 735 (2022).
114. Nguyen, T. D., Mao, S., Yeh, Y., Purohit, P. K. & McAlpine, M. C. Nanoscale flexoelectricity. *Adv. Mater.* **25**, 946 (2013).
115. Vasquez–Sancho, F., Abdollahi, A., Damjanovic, D. & Catalan, G. Flexoelectricity in bones. *Adv. Mater.* **30**, 1705316 (2018).
116. Wang, B., Gu, Y., Zhang, S. & Chen, L.-Q. Flexoelectricity in solids: progress, challenges, and perspectives. *Prog. Mater. Sci.* **106**, 100570 (2019).
117. Xia, Y., Qian, W. & Yang, Y. Advancements and prospects of flexoelectricity. *ACS Appl. Mater. Interfaces* **16**, 9597 (2024).
118. Liang, X. et al. Advancements of flexoelectric materials and their implementations in flexoelectric devices. *Adv. Funct. Mater.* **34**, 2409906 (2024).
119. Jia, X., Guo, R., Chen, J. & Yan, X. Flexoelectric effect in thin films: theory and applications. *Adv. Funct. Mater.* **35**, 2412887 (2024).
120. Gu, Y. et al. Ferroelectric control of spin–orbitronics. *Adv. Funct. Mater.* **34**, 2406444 (2024).
121. Fert, A., Ramesh, R., Garcia, V., Casanova, F. & Bibes, M. Electrical control of magnetism by electric field and current-induced torques. *Rev. Mod. Phys.* **96**, 015005 (2024).
122. Kresse, G. & Furthmüller, J. Efficient iterative schemes for ab initio total-energy calculations using a plane-wave basis set. *Phys. Rev. B* **54**, 11169 (1996).
123. Perdew, J. P., Burke, K. & Ernzerhof, M. Generalized gradient approximation made simple. *Phys. Rev. Lett.* **77**, 3865 (1996).
124. Blöchl, P. E. Projector augmented-wave method. *Phys. Rev. B* **50**, 17953 (1994).
125. Mostofi, A. A. et al. An updated version of wannier90: a tool for obtaining maximally-localised wannier functions. *Comput. Phys. Commun.* **185**, 2309 (2014).
126. Mostofi, A. A. et al. wannier90: a tool for obtaining maximally-localised Wannier functions. *Comput. Phys. Commun.* **178**, 685 (2008).

127. Li, J.-W., Su, G. & Gu, B. Possible room-temperature ferromagnetic semiconductor in monolayer $MnSe_2$ through a metal-semiconductor transition. *Phys. Rev. B* **109**, 134436 (2024).
128. Dong, X.-J., You, J.-Y., Zhang, Z., Gu, B. & Su, G. Great enhancement of Curie temperature and magnetic anisotropy in two-dimensional van der Waals magnetic semiconductor heterostructures. *Phys. Rev. B* **102**, 144443 (2020).
129. Koehler, W. & Wollan, E. Neutron-diffraction study of the magnetic properties of perovskite-like compounds $LaBO_3$. *J. Phys. Chem. Solids* **2**, 100 (1957).
130. Li, J.-W., Su, G. & Gu, B. High temperature ferrimagnetic semiconductors by spin-dependent doping in high temperature antiferromagnets. *npj Comput. Mater.* **10**, 205 (2024).
131. Wu, L., Zhou, L., Zhou, X., Wang, C. & Ji, W. In-plane epitaxy-strain-tuning intralayer and interlayer magnetic coupling in $CrSe_2$ and $CrTe_2$ monolayers and bilayers. *Phys. Rev. B* **106**, l081401 (2022).

Acknowledgements

This work is supported by National Key R&D Program of China (Grant No. 2022YFA1405100), National Natural Science Foundation of China (Grant No. 12074378), Chinese Academy of Sciences (Grants No. YSBR-030, No. JZHKYPT-2021-08, No. XDB33000000). GS was supported in part by the Innovation Program for Quantum Science and Technology under Grant No. 2024ZD03005 NSFC No. 12447101 and CAS.

Author contributions

J.W.L. and B.G. conceived the original ideas and supervised the work. J.W.L. performed the first-principles calculations and data analysis. G.S. joined the data discussions. All authors participated in discussing and editing the manuscripts.

Competing interests

The authors declare no competing interests.

Additional information

Supplementary information The online version contains supplementary material available at https://doi.org/10.1038/s41524-025-01737-9.

Correspondence and requests for materials should be addressed to Gang Su or Bo Gu.